

# Relative position control and coalescence of independent microparticles using ultrasonic waves

Shuang Deng,<sup>1</sup> Kun Jia,<sup>2,a)</sup> Jian Chen,<sup>3</sup> Deqing Mei,<sup>1,a)</sup> and Keji Yang<sup>1</sup>

<sup>1</sup>State Key Laboratory of Fluid Power and Mechatronic Systems, College of Mechanical Engineering, Zhejiang University, 38 Zheda Road, Hangzhou 310027, People's Republic of China

<sup>2</sup>State Key Laboratory for Strength and Vibration of Mechanical Structures, School of Aerospace Engineering, Xi'an Jiaotong University, 28 West Xianning Road, Xi'an 710049, People's Republic of China

<sup>3</sup>School of Mechanical and Aerospace Engineering, Nanyang Technological University, 50 Nanyang Avenue, Singapore 639798

(Received 24 January 2017; accepted 22 April 2017; published online 9 May 2017)

Controlling the relative positions and coalescence of independent cells or microparticles is of particular importance for studying many physical phenomena, biological research, pharmaceutical tests, and chemical material processing. In this work, contactless maneuvering of two independent microparticles initially lying on a rigid surface was performed at a stable levitation height within a water-filled ultrasonic chamber. Three lead zirconate titanate transducers with 2 MHz thickness resonance frequency were obliquely mounted in a homemade device to form a sound field in a half space. By modulating the excitation voltage of a single transducer and the subsequent combination of amplitude and phase modulation, two separate 80  $\mu\text{m}$  diameter silica beads were picked up from the chamber bottom, approached, and then coalesced to form a cluster in different ways. Both particles simultaneously migrated towards each other in the former process, while more dexterous movement with single-particle migration was realized for the other process. There is good agreement between the measured trajectories and theoretical predictions based on the theory of the first-order acoustic radiation force. The method introduced here also has the ability to form a cluster at any desired location in the chamber, which is promising for macromolecule processing ranging from the life sciences to biochemistry and clinical practice. Published by AIP Publishing.

[<http://dx.doi.org/10.1063/1.4983015>]

## I. INTRODUCTION

In multicellular organisms, cell-to-cell communication plays an important role in their response to the environment and individual development, such as proliferation and apoptosis.<sup>1,2</sup> Understanding the mechanism of intercellular signal transduction is essential for pathological and pharmacology research, such as disease diagnostics, immunological reactions, drug screening, cell fusion, and characterization.<sup>1–5</sup> Usually, the intercellular information exchange process is highly related to their relative spatial location. For example, endocrine and paracrine signals can transmit in a noncontact manner between distant cells and targets in the vicinity, respectively, whereas juxtacrine signals are only received by a direct surface interaction.<sup>6</sup> In the area of drug delivery, to understand and develop new therapeutic agents, exhaustive *in vitro* investigation of drug–cell interactions is required before *in vivo* measurements. Controllably and noninvasively transporting the drug carrier (complex molecules,<sup>7</sup> micelles and liposomes,<sup>8</sup> or microbubbles<sup>9</sup>) towards the target cell and then maintaining the drug at the desired relative distance for sufficient time are required to observe the detailed drug–cell interaction process. Conventional chemical and biomedical approaches performed with *in vitro* platforms are often limited to inadequate spatial resolution and controllability,<sup>10</sup> and

consequently, it is not possible to describe the behavior of particle–particle interactions at a certain relative distance. Hence, the ability to dexterously control the location of a single microparticle relative to another and particle coalescence within a fluid are of fundamental importance for investigating the mechanism and pathways of location-dependent interactions in multiple microparticle systems. In addition to these above-mentioned biological research areas, a microparticle localization technique might aid in observing many physical phenomena, such as the dynamic forces between two oil droplets in water<sup>11</sup> or formation of aqueous droplet networks encapsulated within small oil drops.<sup>12</sup>

Since the first demonstration of optical trapping of a single dielectric microparticle in the late 1980s,<sup>13</sup> the applicable objects have been extended to metal particles, cells, bacteria, and semiconductor nanowire,<sup>14–17</sup> making optical tweezers a powerful contactless manipulation technique. Nowadays, more complicated operations have been achieved, such as disrupting protein complexes and then tracking the motor protein with nanometer resolution.<sup>18</sup> Because the heat from focusing a laser with high energy density may result in potential physiological damage, biocompatibility maintains a major concern for this technology.<sup>19–23</sup> However, as its acoustic counterpart, ultrasonic manipulation operated at the same power intensity as ultrasound imaging has been proven to have little impact on the vitality and function of biomaterials.<sup>24</sup> Because of the combination of miniaturization,

<sup>a)</sup>Authors to whom correspondence should be addressed. Electronic addresses: [kunjia@mail.xjtu.edu.cn](mailto:kunjia@mail.xjtu.edu.cn) and [meidq\\_127@zju.edu.cn](mailto:meidq_127@zju.edu.cn)

simplicity, and low cost, acoustic-based microparticle manipulation has attracted increasing interest.

It has been known for a long time that acoustic waves can exert radiation forces on scatterers immersed in air or other fluid media and form traps at spatial locations where these forces converge to a potential minimum.<sup>25–28</sup> In the past decade, diverse applications, including aggregation, separation, and transportation of cells or microparticles, have been investigated not only by focused transducers in an analogous manner to optical tweezers but also by multiplanar transducers,<sup>29–33</sup> which are able to achieve pattern trapping and simultaneously manipulate multiple particles. In our previous studies,<sup>34,35</sup> we performed long-range two-dimensional transportation of microparticles using phase-controllable ultrasonic waves. In this method, the distance between the adjacent acoustic potential minima in the ultrasound field remains constant, meaning that it lacks the ability to adjust the relative positions of the two targets. Controlling both the cell-cell distance and cell arrangement has been achieved in a surface acoustic wave device that uses two pairs of orthogonally arranged interdigital transducers.<sup>36</sup> Two cells initially located within a unit square of pressure antinode lattice can be pushed to the pressure node center under the counterbalance of the acoustic radiation force and acoustic streaming. Because of the inconspicuous mechanism of this manipulation, discrete distance adjustment is only derived. The progress in an ultrasonic phased array may provide an alternative solution.<sup>37–39</sup> A circular ultrasonic array with 64 elements was developed to synthesize a Bessel-function-shaped sound field, in which independent microparticles trapped at the center pressure minimum could be brought together by the reduced trap size.<sup>40</sup> However, the accessible spatial resolution of this method is poor. Moreover, the target microparticles in the above-mentioned studies were all initially suspended in a fluid, and once laid on the bottom surface, the manipulation performance may deteriorate. For overcoming these limitations, the potential minimum of the acoustic radiation force should be formed in three dimensions and regulated in such a way to control the relative distance between two adjacent traps rather than the individual size.

In this study, we propose a contactless ultrasonic method to coalesce two independent microparticles initially lying on a rigid surface without any damage or contamination. The detailed configuration of the homemade setup is described, and the performance of the lead zirconate titanate (PZT) transducers is calibrated to improve the controllability. The working principle of the proposed method is introduced by analyzing the mechanical effects of the pressure amplitude and relative phase modulation using the theory of the primary acoustic radiation force. About 80  $\mu\text{m}$  diameter silica beads are then used to perform coalescence operations in two different ways: dual-particle and single-particle migration. Based on the fact that microparticles are trapped at the pressure nodes, the experimental results are compared with predicted theoretical trajectories. More delicate movement of an individual particle or a coalesced cluster is expected by careful design of the voltage amplitude and phase adjustment.

## II. PROTOTYPE DEVICE

Figure 1(a) shows a schematic diagram of our apparatus, which consists of a Petri dish filled with deionized water, a plastic pedestal, three identical PZT transducers and a multi-channel functional generator, a power amplifier array, and a visual system. The pedestal placed at the center of the Petri dish was fabricated by stereolithography printing with photopolymer Somos GP Plus 14122 (DSM Corporation, The Netherlands). A 10 mm radius steel disk with smooth surfaces is embedded in the pedestal center as a wave reflector. Three PZT transducers with 2 MHz thickness resonance frequency (ChangZhou Ultrasonic Electronics Corporation, China) are obliquely mounted on the pedestal, ensuring that the angle between each incident sound beam and the z axis is 120° and all of the sound beam axes pass through the disk center. The width, height, and thickness of the PZT transducers are 18 mm, 9 mm, and 7 mm, respectively. In the horizontal plane, the angle between the projections of every two sound beam axes is 120° and the distance between the center points of the adjacent transducer radiating surface (16 mm

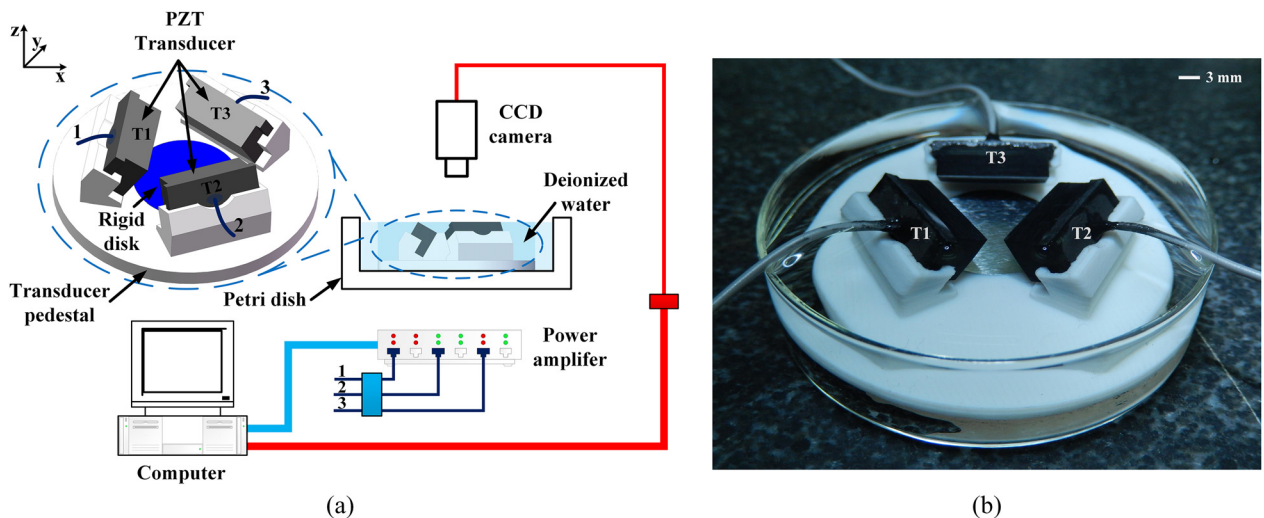


FIG. 1. (a) Schematic illustration and (b) photo of the experimental apparatus for the coalescence of independent microparticles.

TABLE I. Acoustic parameters of deionized water, the steel disk, and the silica beads.

Name	Density(g/cm <sup>3</sup> )	Sound speed (m/s)
Deionized water	1.0	1480
Steel disk	7.98	5664
Silica bead	2.33	5340

$\times 9$  mm) is 14.7 mm. For generating a unidirectional incident wave and minimizing the reflections from the other two transducers, an epoxy matching layer and absorbing backing layer are included in each transducer. After being amplified by the power amplifier array (homemade using PA19, Apex Microtechnology Corporation), continuous sinusoidal voltage signals from a multichannel function generator (homemade PXI platform using FPGA) are applied to the transducers. The amplitude and phase of the actuation signal can be independently adjusted by a computer with a PXI platform (PXIS-2508, ADLINK). A stereoscopic charge-coupled device (CCD) camera (GCO-260202, Daheng Imaging, China) is used to capture the detailed movement of the target microparticle. Figure 1(b) shows the actual apparatus and the related acoustic parameters of deionized water and the steel disk are listed in Table I.

Each PZT transducer in the above-mentioned device is individually calibrated using a needle hydrophone (1376, Precision Acoustics, Ltd., UK) at the given frequency. The hydrophone diameter is small (0.2 mm), which ensures a minimal influence of the scattering field on the measurement. Figure 2 shows the measured pressure for each transducer when the excitation voltage  $V_{pp}$  increases from 0 V to 70 V in steps of 5 V. The consistency of the PZT transducers is satisfactory. It is clear that the generated acoustic pressure increases with increasing excitation voltage and shows good linearity in the range 0 V–60 V. However, output saturation appears at voltages higher than about 60 V, which may be caused by the limitation of the PZT material.

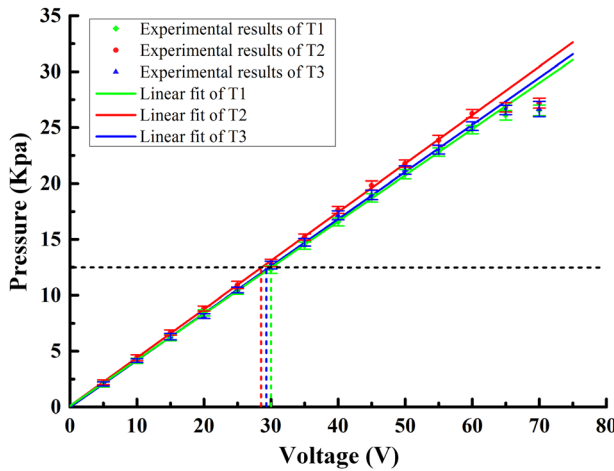


FIG. 2. Measured pressure for each PZT transducer (T1, T2, and T3) when the excitation voltage  $V_{pp}$  increases from 0 to 70 V in steps of 5 V. Each transducer is calibrated using a needle hydrophone at the given frequency of 2 MHz. The circles are the measured pressures, and the solid lines are the linear fits to the experimental measurements.

For improving the device controllability, the maximum excitation voltage was selected to be 60 V (within the linear range). In the following experiments, the calibrated activation voltages were applied to the transducers to obtain the same output pressures. Silica beads (OPS Diagnostics LLC, USA) with a diameter of about 80  $\mu$ m were used as the target microparticles, and their acoustic characteristics are listed in Table I.

### III. WORKING PRINCIPLE

#### A. Theory of the primary acoustic radiation force

With the assumption that the matching layers reflect very small ultrasonic waves, the proposed apparatus can be modeled as three plane waves generated by the PZT transducers within a half-space, as shown in Figure 3. All of the acoustic beams pass through the origin of the coordinate system, and the angles  $\varphi_1$ ,  $\varphi_2$ , and  $\varphi_3$  between the projection of the incident acoustic beam and the  $x$  axis in the horizontal plane are  $0^\circ$ ,  $120^\circ$ , and  $240^\circ$ , respectively. Point  $p(r, \alpha, \beta)$  indicates an arbitrary calculation point for the acoustic radiation force in the spherical coordinate system centered at O, where  $r$  is the distance between the point and O,  $\alpha$  is the azimuth angle measured in the  $x$ - $y$  plane from the  $x$  axis, and  $\beta$  is the polar angle measured from the  $z$  axis. Because a steel disk is embedded on the platform bottom and can be treated as a sound hard boundary, three totally reflected waves with identical amplitude will be generated. Thus, the total sound field  $P_t$  in the fluid can be written as

$$P_t = 2 \cos(\vec{k}^v \cdot \vec{\varsigma}) \sum_{j=1}^3 A_j \exp\left[(\vec{k}_j^h \cdot \vec{l} + \gamma_j)\right], \quad (1)$$

where  $\vec{k}^v$  and  $\vec{k}_j^h$  are the vertical and horizontal components of the wave number vector,  $A_j$  are the pressure amplitudes,  $\vec{r}$  is the position vector,  $\gamma_j$  is for the initial phases,  $\vec{\varsigma}$  and  $\vec{l}$  are the projections of  $\vec{r}$  in the  $z$  axis and  $x$ - $y$  plane, respectively.

Microparticles immersed in a sound field will experience a time-independent radiation force, which has been

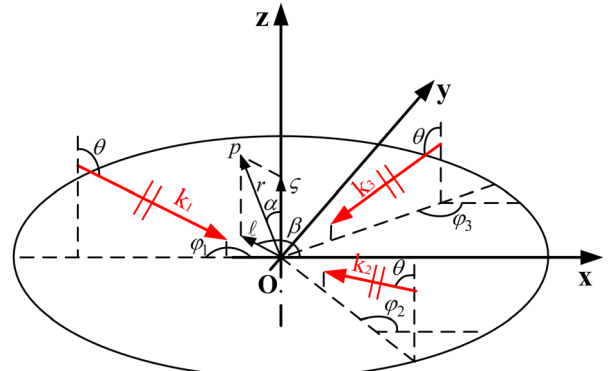


FIG. 3. Simplified model of our homemade apparatus. Three plane waves generated from the PZT transducers are obliquely incident on the steel disk, which can be treated as a sound hard boundary. The angles  $\varphi_1$ ,  $\varphi_2$ , and  $\varphi_3$  between each acoustic beam and the  $x$  axis in the horizontal plane are  $0^\circ$ ,  $120^\circ$ , and  $240^\circ$ , respectively. The coordinate of the arbitrary calculation point  $p$  is  $(r, \alpha, \beta)$  in the spherical coordinate system centered at O.

investigated by many researchers.<sup>25–28</sup> In our device, the target size is much smaller than the ultrasonic wave wavelength and deionized water with a very low viscosity can be regarded as an ideal fluid. According to our previous theoretical study,<sup>41</sup> the acoustic radiation force on any microparticle in any arbitrary sound field can be calculated by

$$\vec{F} = \left\langle \oint_{f_0} \left\{ \left[ \frac{1}{2} \rho_0 v^2 - \frac{1}{2c_0^2} \rho_0 \left( \frac{\partial \Phi}{\partial t} \right)^2 \right] \vec{n} - \rho_0 \vec{v} (\vec{v} \cdot \vec{n}) \right\} df \right\rangle, \quad (2)$$

where  $\rho_0$  is the density of the medium,  $\vec{v}$  is the velocity of the medium,  $c_0$  is the speed of sound in the medium,  $\Phi$  is the

total velocity potential, and  $\vec{n}$  is the outward unit normal vector of  $df$ . As proposed in a number of previous studies,<sup>25–28</sup> the particles are trapped at the pressure nodes of the sound field and migrate with them.

According to Eq. (1), the nodal positions in any vertical line and the horizontal slice can be conveniently determined by the respective components

$$\cos(\vec{k}^h \cdot \vec{\zeta}) = 0 \quad \text{and} \quad \sum_{j=1}^3 A_j \exp \left[ i(\vec{k}_j^h \cdot \vec{\ell} + \gamma_j) \right] = 0.$$

For any nodal position, the spatial coordinates are a function of the incident wave amplitude and phase,

$$\begin{cases} \varsigma = \frac{1+2m}{4} \lambda_v \\ \left( \vec{k}_2^h \cdot \vec{\ell} + \gamma_2 \right) - \left( \vec{k}_1^h \cdot \vec{\ell} + \gamma_1 \right) = \pm \left[ \pi - \arccos \left( \frac{A_1^2 + A_2^2 - A_3^2}{2A_1 A_2} \right) \right] + 2n_1 \pi \quad (m, n_1, n_2 = 0, \pm 1, \pm 2, \dots) \\ \left( \vec{k}_3^h \cdot \vec{\ell} + \gamma_3 \right) - \left( \vec{k}_2^h \cdot \vec{\ell} + \gamma_2 \right) = \pm \left[ \arccos \left( \frac{A_1^2 + A_2^2 - A_3^2}{2A_1 A_2} \right) + \arccos \left( \frac{A_1^2 + A_3^2 - A_2^2}{2A_1 A_3} \right) \right] + 2n_2 \pi. \end{cases} \quad (3)$$

It is clear that the vertical positions are only related to the equivalent vertical wavelength  $\lambda_v$ , whereas the horizontal components are determined by the amplitudes  $A_j$  and phases  $\gamma_j$  of all three waves. Thus, the particles trapped in the pressure nodes can migrate in the horizontal plane by adjusting the latter two parameters while maintaining their levitation height.

## B. Effect of amplitude modulation

Figure 4(a) shows the  $x$ - $y$  plane distribution of the normalized pressure field for the incident waves with identical amplitudes  $A_0$  and constant initial phases ( $-\pi$ ,  $0$ , and  $0$  for  $\gamma_1$ ,  $\gamma_2$ , and  $\gamma_3$ , respectively). The blue contours indicate the pressure minima and the red contours represent the pressure maxima. When the excitation voltage of transducer T1 is changed by  $\Delta V_1$ , the amplitude of the corresponding plane wave changes by  $\Delta A_1$ . From Eq. (3), we can deduce that the migrations of the pressure nodes in the  $x$  and  $y$  directions are

$$\begin{cases} \Delta x = 0 \\ \Delta y = \pm \frac{\sqrt{3}}{3\pi} \left[ \arccos \left( \frac{1}{2} + \frac{\Delta A_1}{2A_0} \right) - \frac{\pi}{3} \right] \lambda_h, \end{cases} \quad (4)$$

where  $\lambda_h$  is the equivalent horizontal wavelength. Apparently, the pressure nodes only move along the  $y$  axis. With an increase of  $\Delta A_1$ , the pressure node marked by the green dot migrates in the  $-y$  direction while the other node travels the same distance but in the  $+y$  direction, and *vice versa*. Figures 4(b)–4(d) shows the distributions of the sound pressure when the pressure amplitude  $A_1$  is changed to  $A_0/2$ ,  $3A_0/2$ , and  $2A_0$ , respectively. The initially separate pressure

nodes simultaneously move toward each other by increasing the ratio of  $A_1/A_{2\text{or}3}$ , and they finally reach a distance smaller than the particle diameter. Consequently, the two particles independently trapped in adjacent pressure nodes will migrate in opposite directions and coalesce during this amplitude modulating operation.

Figures 5(a)–5(d) show the corresponding pressure contours in the vertical plane passing through the pressure nodes. The pressure nodes approach each other along the  $y$  axis, and their fixed height indicated by the dashed lines is  $\lambda_v/4$  above the rigid surface, as predicted by the first equation of Eq. (3).

## C. Combination of amplitude and phase modulation

Now, we take into account wave phase  $\gamma_j$  in Eq. (3). For the case with identical and constant pressure amplitudes, the horizontal movement of the pressure nodes related to phase variation  $\Delta\gamma_j$  can be obtained from Eq. (3),

$$\begin{cases} \Delta x = \frac{1}{6\pi} (\Delta\gamma_2 + \Delta\gamma_3 - 2\Delta\gamma_1) \lambda_h \\ \Delta y = \frac{\sqrt{3}}{6\pi} (\Delta\gamma_3 - \Delta\gamma_2) \lambda_h. \end{cases} \quad (5)$$

From this relationship, it is clear that all of the pressure nodes move along the individual sound beam axis with corresponding phase modulation. An arbitrary trajectory can be achieved by varying the phases of all of the waves. As Eq. (3) is a linear system, superimposition is applicable for controlling the  $x$ - $y$  plane nodal positions, and dexterous migration of the adjacent pressure nodes can be achieved by appropriate amplitude and phase modulation.

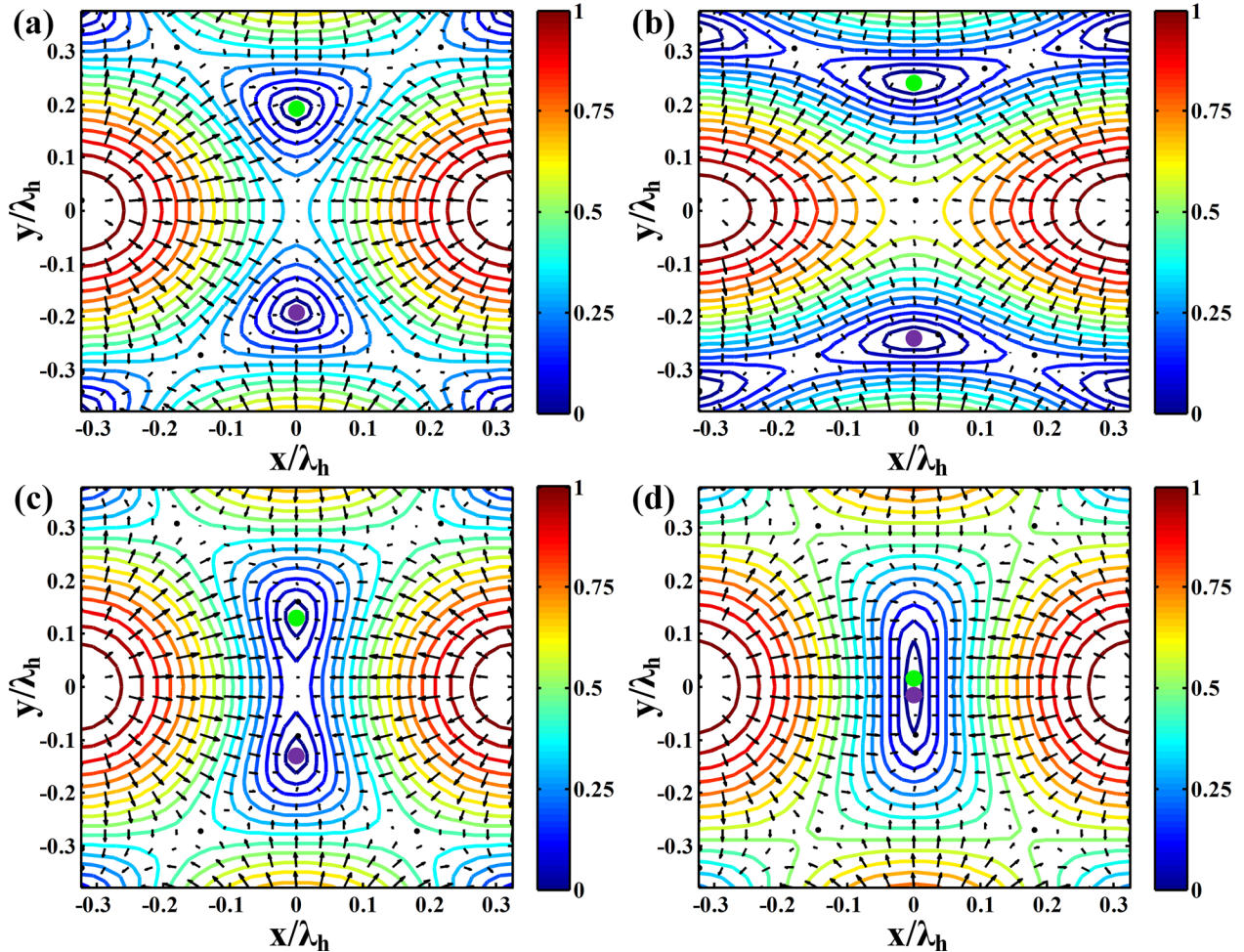


FIG. 4. Distribution of the normalized pressure field in the horizontal plane resulting from superposition of three incident and reflected waves under different pressure amplitudes but constant phases ( $-\pi$ , 0, and 0 for  $\gamma_1$ ,  $\gamma_2$ , and  $\gamma_3$ , respectively). The length of the arrows is proportional to the magnitude of the acoustic radiation force, while the orientation of the arrow indicates the direction of the force. (a)  $A_1 = A_0$ , (b)  $A_1 = A_0/2$ , (c)  $A_1 = 3A_0/2$ , and (d)  $A_1 = 2A_0$ .

By adjusting the wave amplitude by  $\Delta A_1$ , as mentioned in Section III B, and using the phase variation

$$\begin{cases} \Delta\gamma_1 = 0 \\ \Delta\gamma_2 = -\frac{\pi}{3} + \arccos\left(\frac{1}{2} + \frac{\Delta A_1}{2A_0}\right), \\ \Delta\gamma_3 = \frac{\pi}{3} - \arccos\left(\frac{1}{2} + \frac{\Delta A_1}{2A_0}\right) \end{cases} \quad (6)$$

the  $+y$  direction movement of the violet pressured node in Figure 4, which is related to the amplitude modulation effect, will be counteracted by the  $-y$  direction migration resulting from the above phase modulation. In contrast, the displacement of the other pressure node doubles along the  $-y$  direction. Figures 6(a)–6(d) shows the detailed transformation of the pressure field, and single pressure node migration is achieved in this condition.

#### IV. EXPERIMENTAL RESULTS AND DISCUSSION

##### A. Dual-particle migration

At the beginning, there is no sound field established and the two silica beads are lying on the upper surface of the steel disk. Transducers T2 and T3 are then excited with the

voltages indicated in Figure 2 (28 and 29 V, respectively), while the voltage applied to transducer T1 is set at 5 V. After this operation, both of the silica beads are picked up from the rigid surface and stably trapped in the fluid at a height of  $251 \mu\text{m}$  under the mechanical effect of the ultrasonic field, as shown in Figure 7(a). A detachment of the microparticles from the rigid surface is encouraging, especially for applications in which the targets are easily damaged or contaminated. Compared with the distance of  $463 \mu\text{m}$  between the particles along the  $y$  axis, the distance along the  $x$  axis is very small ( $3 \mu\text{m}$ ), so it is assumed that the two particles are arranged parallel to the  $y$  axis. As long as the actuation voltage is kept constant, there is no obvious variation in the suspending height and relative distance. Once the voltage of transducer T1 is lower than 5 V, the silica beads fall into an unstable state.

By increasing the excitation voltage of transducer T1 from 5 to 60 V while keeping the signal phases of transducers T1, T2, and T3 fixed at  $-\pi$ , 0, and 0, respectively, the two separate particles start to migrate toward each other. Figures 7(b)–7(d) show the relative positions of the silica beads with 25, 45, and 60 V actuation voltages of transducer T1, respectively. The detailed  $x$ - $y$  plane movement is shown in Figure 8 with a 10 V voltage interval for steps a–d and a

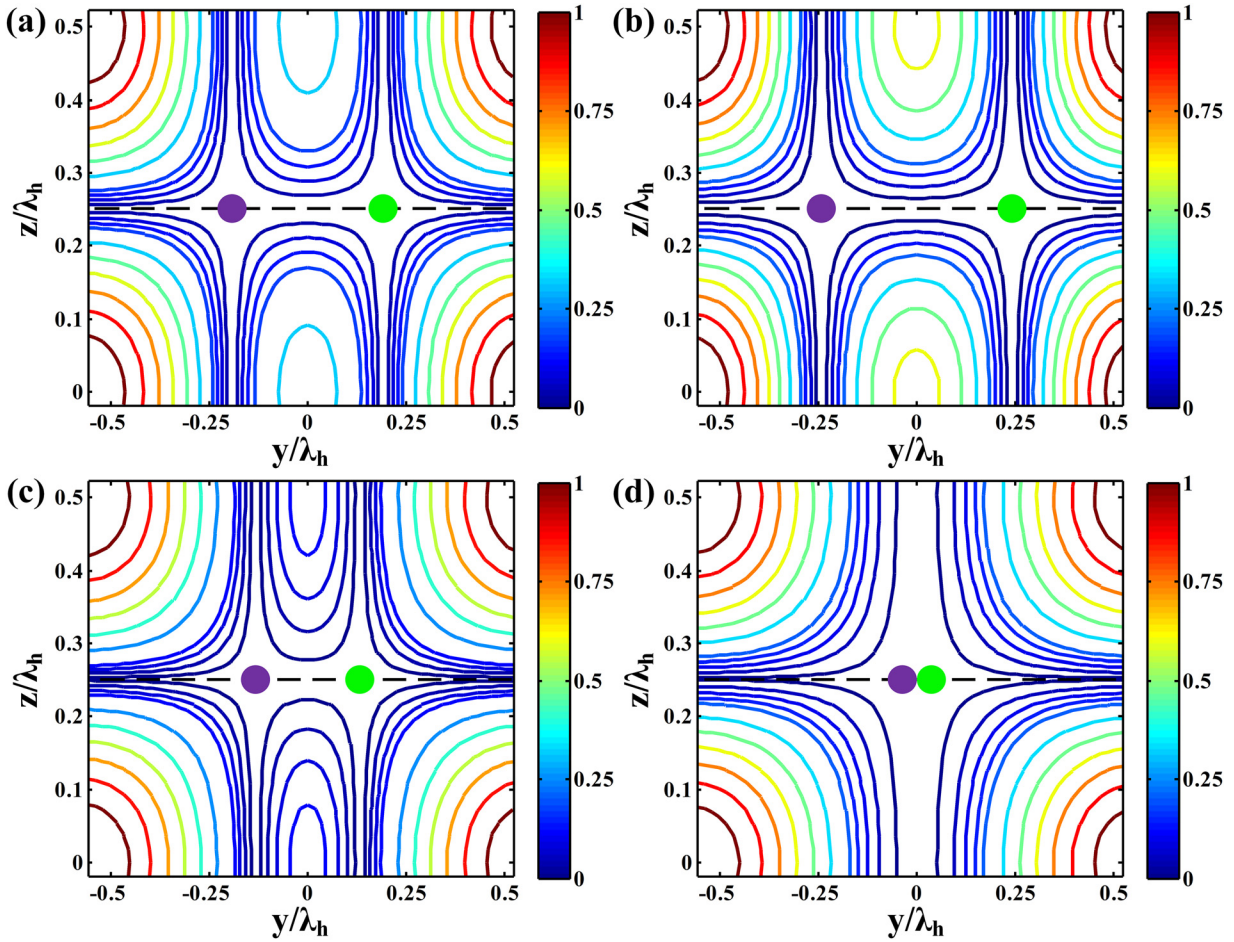


FIG. 5. Corresponding acoustic pressure contours in the vertical plane passing through the pressure nodes in Figures 4(a)–4(d). The height of the vertical pressure nodes remains the same, although the horizontal pressure nodes are shifted.

5 V voltage interval for steps d–i. Gradually increasing the voltage of transducer T1 only introduces relative movement along the  $y$ -axis, and the two silica beads are ultimately brought into contact at the center position marked by the red dot-dashed line in Figure 8(i).

For quantifying the trajectories of the two silica beads in the coalescence process, a series of images were captured from the side and top by CCD cameras, and the particle profiles were extracted from each picture by image processing technology. The time interval between each step was about 5 s, and the total movement took about 2 min. Figure 9(a) shows the superimposition of seven processed frames in the  $x$ - $y$  plane. The center positions of the migrating particles during the movement are marked by green and violet circles. We may find that the particles fluctuate in the direction perpendicular to the travelling path and the maximum deviation is about 28  $\mu\text{m}$ , as indicated by the dashed lines.

Figures 9(b)–9(d) show the relationship between the measured particle positions and the amplitude of the sinusoidal voltage of transducer T1. As shown in Figure 9(b), the position fluctuation along the  $x$  axis becomes obvious when the excitation voltage exceeds 45 V and reaches the maximum value just before coalescence. From Figure 9(c), the  $y$ -axis distance between the two beads remains approximately 80  $\mu\text{m}$  for excitation voltages larger than 55 V, which means that the initially separate particles are in contact. It is

interesting that the relative movement along the  $y$  axis is almost symmetric with respect to the center line until particle coalescence occurs. However, the right particle is attracted to the left particle in the transient collision process, breaking the symmetry. The  $z$ -axis positions in Figure 9(d) show that the silica beads can be stably levitated, although the mechanical effect of the ultrasound wave strengthens with increasing excitation voltage.

According to the calibrated voltage–pressure relationship in Figure 2, the theoretical  $x$ -axis and  $y$ -axis nodal positions for dual-particle migration can be predicted by Eq. (3), and they are shown as lines in Figures 9(b)–9(d). Because of the gravity, the average suspending height is about 251  $\mu\text{m}$  less than the theoretical value of 370  $\mu\text{m}$  and the maximum fluctuation during migration and coalescence is less than 6  $\mu\text{m}$ . When the distance between the two silica beads is two times larger than the particle diameter, the measured trajectories show good agreement with the theoretical calculations. However, further decreasing the distance results in clear deviations, especially in the  $x$ -axis positions, which may be caused by acoustical interaction between the silica beads. The microparticles immersed in the acoustic field not only experience the primary radiation force, but they are also affected by the second-order Bjerknes force resulting from mutual scattering. From the above measurements, we can conclude that the influence of the second-order Bjerknes

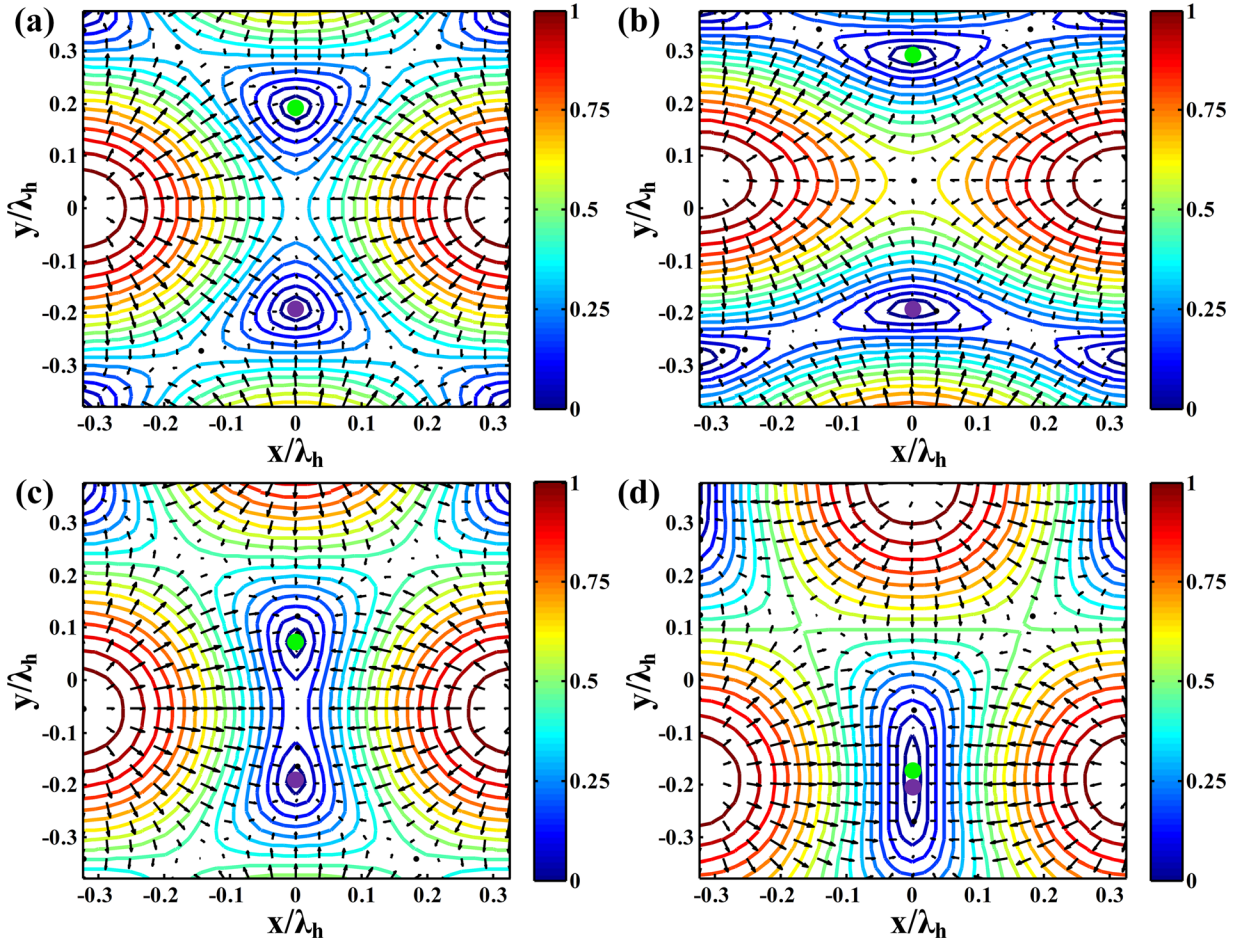


FIG. 6. Distribution of the normalized pressure field in the horizontal plane under different pressure amplitudes taking account of wave phase compensation. (a)  $A_1 = A_0$ ,  $\gamma_1 = -\pi$ ,  $\gamma_2 = 0$ ,  $\gamma_3 = 0$ . (b)  $A_1 = A_0/2$ ,  $\gamma_1 = -\pi$ ,  $\gamma_2 = 0.086\pi$ ,  $\gamma_3 = -0.086\pi$ . (c)  $A_1 = 3A_0/2$ ,  $\gamma_1 = -\pi$ ,  $\gamma_2 = -0.103\pi$ ,  $\gamma_3 = 0.103\pi$ . (d)  $A_1 = 2A_0$ ,  $\gamma_1 = -\pi$ ,  $\gamma_2 = -0.333\pi$ ,  $\gamma_3 = 0.333\pi$ .

force starts to play a significant role for distances less than three times the microparticle diameter (about 240  $\mu\text{m}$ ).

It is interesting that particle coalescence actually occurs before the theoretically predicted moment, which can be attributed to the following reason. When the excitation voltage of transducer T1 is 55 V, the amplitude of the generated plane wave is about twice that of the other two transducers and the pressure contours around the two nodes form a narrow

trapping region, as shown in Figure 4(d). In this condition, the constraint of the primary acoustic radiation force within the trapping region is not strong enough, and one of the particles may be attracted by the other and break away from its local constraint under the effect of the second-order Bjerknes force. Considering the relatively small force magnitude and traveling path, the particle velocity during the coalescence process is very small and fragile targets will not be damaged.

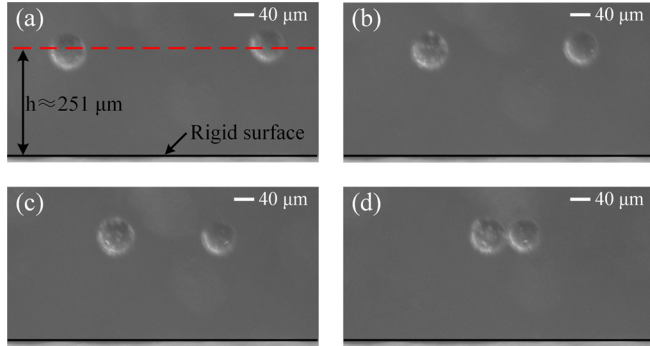


FIG. 7. Relative position control and coalescence of two silica beads achieved by modulating the actuation voltage applied to transducer T1: (a) 5 V, (b) 25 V, (c) 45 V, and (d) 60 V. The particles are picked up from the rigid surface and stably trapped in the fluid medium at a height of 251  $\mu\text{m}$  under the mechanical effect of the ultrasonic field.

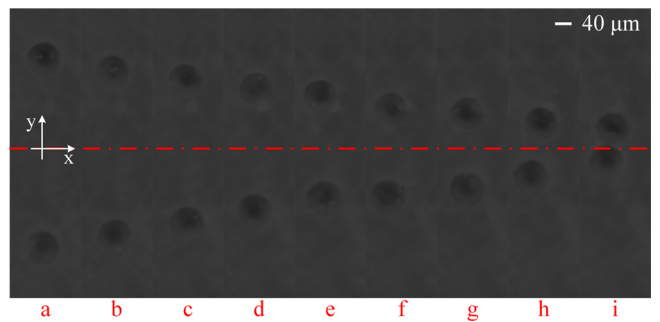


FIG. 8. Detailed process of dual-particle migration in the  $xy$  plane. Two separate particles migrate together and ultimately come into contact at the center position marked by the red dot-dashed line when the electric excitation of transducer T1 increases from 5 V to 60 V. The electric excitation of transducer T1 varies in 10 V voltage intervals for steps a–d and 5 V voltage intervals for steps (d)–(i).

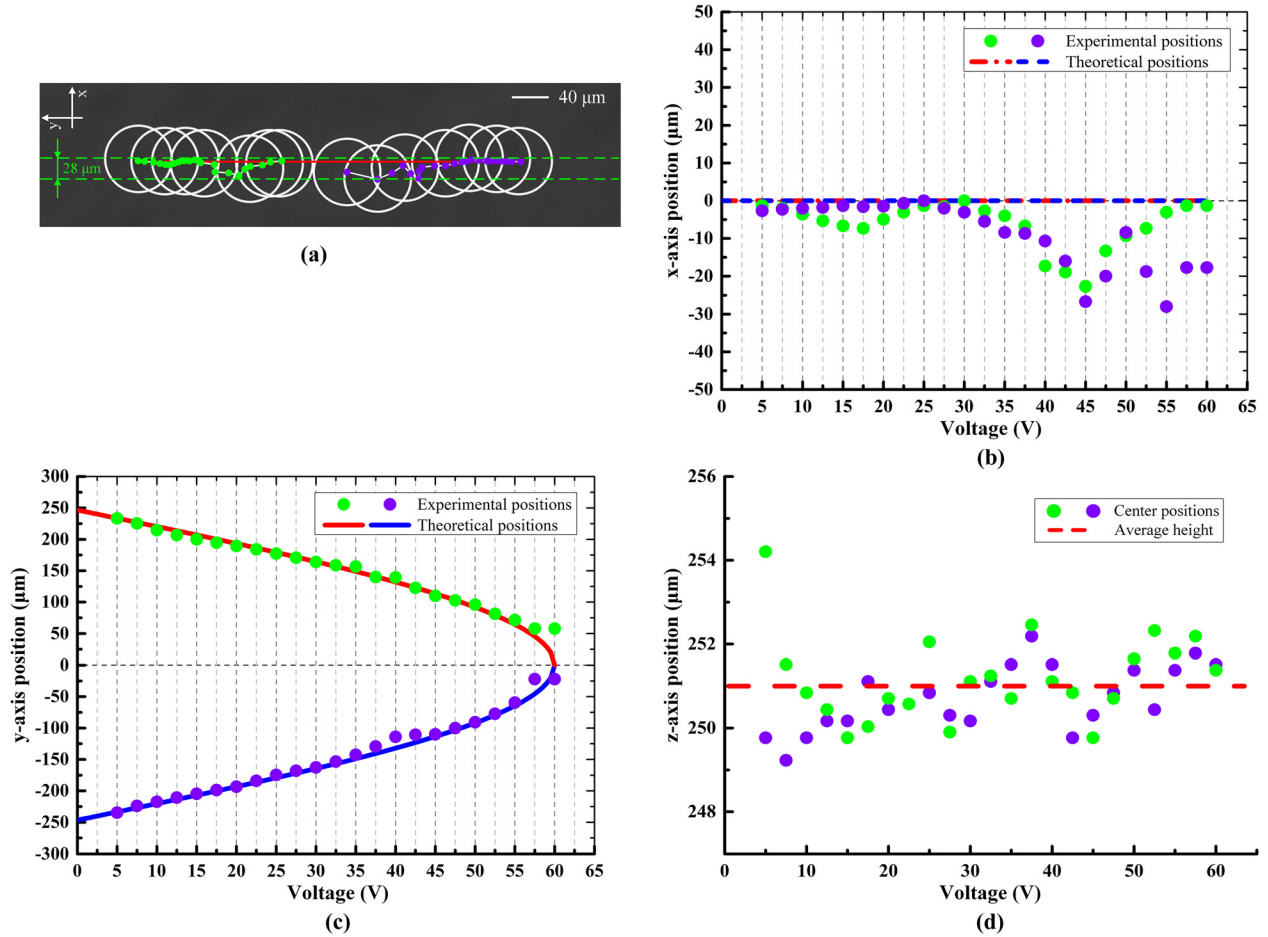


FIG. 9. (a) Trajectories of the silica beads in the dual-particle migration process obtained by superposing seven processed frames in the *xy* plane. The green and violet circles indicate the center positions of the two silica beads. (b) Experimental and theoretical relationships between the *x*-axis particle positions and the actuation amplitude of transducer T1. The solid circles indicate the measured positions of the two silica beads in the *x*-axis direction and the lines are the theoretical positions. (c) *y*-axis position versus the sinusoidal voltage. (d) *z*-axis position versus the sinusoidal voltage. The silica beads are stably levitated at a height of about 251 μm and the maximum fluctuation during migration and coalescence is less than 6 μm.

## B. Single-particle migration

When the relative phase of the sinusoidal signals applied to the transducers is taken into account along with voltage amplitude modulation, the coalescence operation can be made more flexible. Figure 10 shows an alternative implementation with the same sized particles used in the dual-particle migration. It is clear that the upper particle gradually moves toward the lower particle, crosses the center line, and

finally comes into contact with the lower particle. During the whole process, the lower particle almost maintains its initial position. For this movement, the related excitation parameters of the transducers are sequentially listed in Table II. The illustrated coalescence process with single-particle migration

TABLE II. Excitation voltage and phase applied to the three PZT transducers.

	$V_1$ (V)	$V_2$ (V)	$V_3$ (V)	$\varphi_{1t}^a$	$\varphi_{2t}^a$	$\varphi_{3t}^a$
a	5	28	29	$-\pi$	$0.14\pi$	$-0.14\pi$
b	10	28	29	$-\pi$	$0.113\pi$	$-0.113\pi$
c	15	28	29	$-\pi$	$0.086\pi$	$-0.086\pi$
d	20	28	29	$-\pi$	$0.058\pi$	$-0.058\pi$
e	25	28	29	$-\pi$	$0.03\pi$	$-0.03\pi$
f	30	28	29	$-\pi$	0	0
g	35	28	29	$-\pi$	$-0.032\pi$	$0.032\pi$
h	40	28	29	$-\pi$	$-0.066\pi$	$0.066\pi$
i	45	28	29	$-\pi$	$-0.103\pi$	$0.103\pi$
j	50	28	29	$-\pi$	$-0.147\pi$	$0.147\pi$
k	55	28	29	$-\pi$	$-0.202\pi$	$0.202\pi$
l	60	28	29	$-\pi$	$-0.333\pi$	$0.333\pi$

<sup>a</sup> $\varphi_{jt}$  is the total phase applied to the *j*th transducer, including the initial phase and phase compensation.

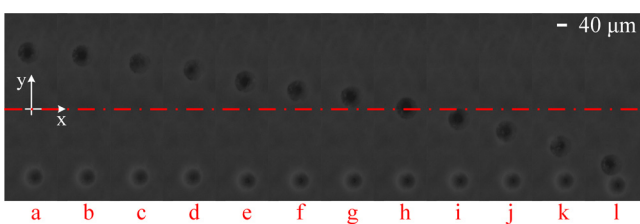


FIG. 10. Detailed process of single-particle migration in the *xy* plane. When the relative phases of the sinusoidal signals applied to the transducers are taken into account along with voltage amplitude modulation, the upper particle gradually moves toward the lower particle, crosses the center line, and finally comes into contact with the lower particle, which almost maintains its initial position. The related excitation parameters of the transducers for each moment are sequentially listed in Table II.

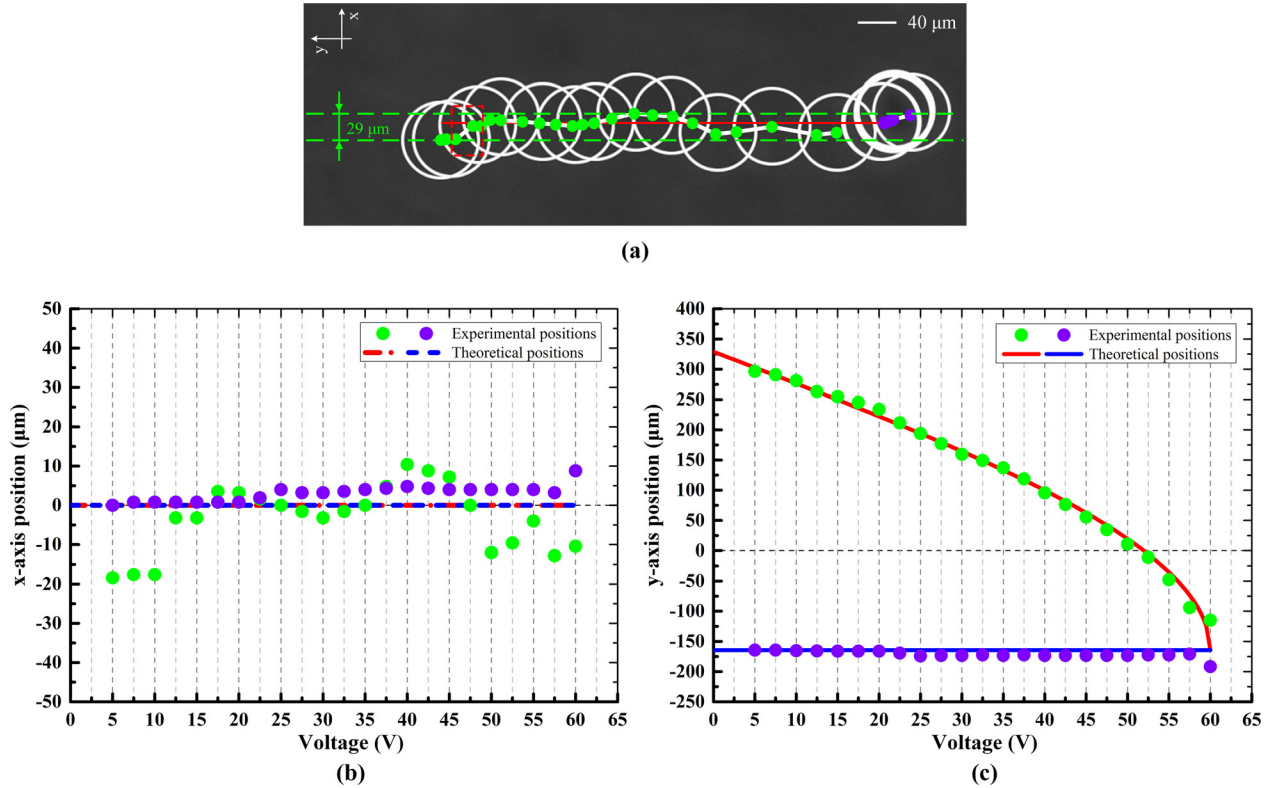


FIG. 11. (a) Trajectories in the single-particle migration process. The green and violet circles indicate the center positions of the two silica beads. (b) Experimental and theoretical relationships between the  $x$ -axis particle position and the actuation amplitude of transducer T1. (c)  $y$ -axis position versus the sinusoidal voltage.

is very attractive for health diagnostics and medicine tests, where *in situ* measurement or *in situ* assembly is required.

For analyzing the detailed movements, a series of images were captured with a 2.5 V voltage interval, as well as the corresponding phase compensation. The  $x$ - $y$  plane trajectories of both particles are shown in Figure 11(a), where the particle that is expected to be stationary (violet circles) slightly fluctuates and the mobile particle (green circles) nearly travels the whole distance. Position fluctuation along the  $x$ -axis also occurs during the transition and the maximum fluctuation is about 29  $\mu\text{m}$ , which is the same level as dual-particle migration. From the relationship between the measured spatial positions and the voltage amplitude of transducer T1 shown in Figures 11(b) and 11(c), the initial  $y$ -axis distance between the particles is about 461  $\mu\text{m}$ , which is in good agreement with the value measured in dual-particle migration, and the two particles are brought into contact with an excitation voltage of 55 V. The threshold voltage for coalescence is the same as that applied in dual-particle migration, although the coalesced cluster moves along the  $-y$ -direction when the excitation voltage increases to 60 V. In addition, migration of silica bead occurs at the same height as dual-particle migration, so the mechanical effect of the ultrasonic field along the  $z$  axis will not be affected by phase modulation.

The theoretical trajectory for single-particle migration is shown in Figures 11(b) and 11(c). In general, there is good agreement between the actual trajectories and the predictions. However, the  $x$ -axis deviation exceeds the average level not only at the stage where the second-order Bjerknes

force becomes important but also at the beginning of migration. A possible explanation is that the constraint of the sound field in the  $x$ -axis direction is relatively weak when the excitation voltage of transducer T1 is much smaller than those applied to the other two transducers, as shown in Figure 6(b). In this case, any disturbances (e.g., micro- or macroacoustic streaming) could drag the silica bead away from the theoretical position. With an increase of the excitation voltage, the silica bead will be pulled back because of the strengthened constraint force, and this restoration process is indicated by a rectangular box in Figure 11(a). As the relative displacement between the two particles at each step is the same as that in dual-particle migration, coalescence still occurs at a voltage of about 55 V. However, amplitude modulation fails to work after particle coalescence, and the cluster continues migrating along the  $-y$  direction under the effect of phase modulation and can be delivered to any desired position.

## V. CONCLUSIONS

Contactless relative position control and coalescence of two independent microparticles have been realized at a stable levitation height within our homemade ultrasonic chamber. By using three oblique incident plane waves and a hard reflector, microparticles initially lying on a surface can be simultaneously picked up and moved towards each other by modulating the amplitude of the excitation voltage. With a combination of amplitude and phase modulation, a cluster can be formed by dexterous single-particle migration and

then transported to any desired position. Dual- and single-particle migration were analyzed by characterizing the corresponding sound field. The theory of the first-order acoustic radiation force predicts the particle trajectories well. From the small deviation occurring before particle coalescence, we can conclude that second order Bjerke's force related to mutual scattering starts to influence the proposed operation when the relative distance between the two particles is less than three times their diameter. The method proposed in this paper may provide a potential tool for material processing in life sciences, polymer chemistry, and drug delivery.

## ACKNOWLEDGMENTS

This work was supported by NSFC (Grant Nos. 11402186 and 51675480) and the China Postdoctoral Science Foundation (Grant No. 2015M572548).

- <sup>1</sup>N. M. Kumar and N. B. Gilula, *Cell* **84**, 381 (1996).
- <sup>2</sup>J. El-Ali, P. K. Sorger, and K. F. Jensen, *Nature* **442**, 403 (2006).
- <sup>3</sup>T. Pawson, *Nature* **373**, 573 (1995).
- <sup>4</sup>J. B. Hupp and M. M. Davis, *Nat. Rev. Immunol.* **3**, 973 (2003).
- <sup>5</sup>E. A. Clark and J. S. Brugge, *Science* **268**, 233 (1995).
- <sup>6</sup>B. N. Manz and J. T. Groves, *Nat. Rev. Mol. Cell Biol.* **11**, 342 (2010).
- <sup>7</sup>D. Gourevich, Y. Hertzberg, A. Volovick, Y. Shafran, G. Navon, S. Cochran, and A. Melzer, *Ultrasound Med. Biol.* **39**, 507 (2013).
- <sup>8</sup>J.-W. Yoo, N. Doshi, and S. Mitragotri, *Adv. Drug Deliv. Rev.* **63**, 1247 (2011).
- <sup>9</sup>J. Castle, M. Butts, A. Healey, K. Kent, M. Marino, and S. B. Feinstein, *Am. J. Physiol. Heart Circ. Physiol.* **304**, H350 (2013).
- <sup>10</sup>F. Guo, J. B. French, P. Li, H. Zhao, C. Y. Chan, J. R. Fick, S. J. Benkovic, and T. J. Huang, *Lab Chip* **13**, 3152 (2013).
- <sup>11</sup>R. R. Dagastine, R. Manica, S. L. Carnie, D. Y. C. Chan, G. W. Stevens, and F. Grieser, *Science* **313**, 210 (2006).
- <sup>12</sup>G. Villar, A. J. Heron, and H. Bayley, *Nat. Nanotechnol.* **6**, 803 (2011).
- <sup>13</sup>A. Ashkin, J. M. Dziedzic, J. E. Bjorkholm, and S. Chu, *Opt. Lett.* **11**, 288 (1986).
- <sup>14</sup>K. Dholakia and T. Čižmár, *Nat. Photonics* **5**, 335 (2011).
- <sup>15</sup>X. Zhang, K. Halvorsen, C.-Z. Zhang, W. P. Wong, and T. A. Springer, *Science* **324**, 1330 (2009).
- <sup>16</sup>A. H. J. Yang, S. D. Moore, B. S. Schmidt, M. Klug, M. Lipson, and D. Erickson, *Nature* **457**, 71 (2009).
- <sup>17</sup>R. Agarwal, K. Ladavac, Y. Roichman, G. Yu, C. M. Lieber, and D. G. Grier, *Opt. Express* **13**, 8906 (2005).
- <sup>18</sup>M. Soltani, J. Lin, R. A. Forties, J. T. Inman, S. N. Saraf, R. M. Fulbright, M. Lipson, and M. D. Wang, *Nat. Nanotechnol.* **9**, 448 (2014).
- <sup>19</sup>H. Zhang and K.-K. Liu, *J. R. Soc. Interface* **5**, 671 (2008).
- <sup>20</sup>Y. Liu, D. K. Cheng, G. J. Sonek, M. W. Berns, C. F. Chapman, and B. J. Tromberg, *Biophys. J.* **68**, 2137 (1995).
- <sup>21</sup>E. J. G. Peterman, F. Gittes, and C. F. Schmidt, *Biophys. J.* **84**, 1308 (2003).
- <sup>22</sup>S. Ayano, Y. Wakamoto, S. Yamashita, and K. Yasuda, *Biochem. Biophys. Res. Commun.* **350**, 678 (2006).
- <sup>23</sup>M. B. Rasmussen, L. B. Oddershede, and H. Siegumfeldt, *Appl. Environ. Microbiol.* **74**, 2441 (2008).
- <sup>24</sup>X. Ding, Z. Peng, S.-C. S. Lin, M. Geri, S. Lie, P. Li, Y. Chena, M. Dao, S. Suresh, and T. J. Huang, *Proc. Natl. Acad. Sci. U.S.A.* **111**, 12992 (2014).
- <sup>25</sup>L. V. King, *Proc. R. Soc. London* **147**, 212 (1934).
- <sup>26</sup>K. Yosioka and Y. Kawasima, *Acustica* **5**, 167 (1995).
- <sup>27</sup>L. P. Gor'kov, Sov. Phys. Dokl. **6**, 773 (1962).
- <sup>28</sup>A. A. Doinikov, *J. Acoust. Soc. Am.* **101**, 713 (1997).
- <sup>29</sup>J. Lee, S.-Y. Teh, A. Lee, H. H. Kim, C. Lee, and K. K. Shung, *Appl. Phys. Lett.* **95**, 073701 (2009).
- <sup>30</sup>Z. Y. Hong, W. J. Xie, and B. Wei, *J. Appl. Phys.* **107**, 014901 (2010).
- <sup>31</sup>J. Lee, C. Lee, H. H. Kim, A. Jakob, R. Lemor, S.-Y. Teh, A. Lee, and K. K. Shung, *Biotechnol. Bioeng.* **108**, 1643 (2011).
- <sup>32</sup>T. Kozuka, T. Tuziuti, H. Mitome, and T. Fukuda, *Jpn. J. Appl. Phys., Part 1* **37**, 2974 (1998).
- <sup>33</sup>P. Glynne-Jones, C. E. M. Démoré, C. Ye, Y. Qiu, S. Cochran, and M. Hill, *IEEE Trans. Ultrason. Ferroelectr. Freq. Control* **59**, 1258 (2012).
- <sup>34</sup>K. Jia, K. Yang, and D. Mei, *J. Appl. Phys.* **112**, 054908 (2012).
- <sup>35</sup>J. Meng, D. Mei, K. Yang, and Z. Fan, *J. Appl. Phys.* **116**, 064909 (2014).
- <sup>36</sup>F. Guo, P. Lia, J. B. French, Z. Mao, H. Zhao, S. Li, N. Nama, J. R. Fick, S. J. Benkovic, and T. J. Huang, *Proc. Natl. Acad. Sci. U.S.A.* **112**, 43 (2015).
- <sup>37</sup>D. Foresti, M. Nabavi, M. Klingauf, A. Ferrari, and D. Poulikakos, *Proc. Natl. Acad. Sci. U.S.A.* **110**, 12549 (2013).
- <sup>38</sup>C. Yoon, B. J. Kang, C. Lee, H. H. Kim, and K. K. Shung, *Appl. Phys. Lett.* **105**, 214103 (2014).
- <sup>39</sup>A. Marzo, S. A. Seah, B. W. Drinkwater, D. R. Sahoo, B. Long, and S. Subramanian, *Nat. Commun.* **6**, 8661 (2015).
- <sup>40</sup>C. R. P. Courtney, C. E. M. Demore, H. Wu, A. Grinenko, P. D. Wilcox, S. Cochran, and B. W. Drinkwater, *Appl. Phys. Lett.* **104**, 154103 (2014).
- <sup>41</sup>Z. Fan, D. Mei, K. Yang, and Z. Chen, *J. Acoust. Soc. Am.* **124**, 2727 (2008).